3D Maxwell's equations and orthogonal nonconforming meshes: a hp-type Discontinuous Galerkin method

Nicolas Canouet, Loula Fezoui, Serge Piperno

INRIA

INSTITUT NATIONAL DE RECHERCHE EN INFORMATIQUE ET EN AUTOMATIQUE

3D Maxwell's equations and orthogonal nonconforming meshes: a hp-type Discontinuous Galerkin method

Nicolas Canouet — Loula Fezoui — Serge Piperno

N° 4912

Août 2003

THÈME 4

ISSN 0249-6399 ISRN INRIA/RR--4912--FR+ENG

INRIA
SOPHIA ANTIPOLIS

3D Maxwell's equations and orthogonal nonconforming meshes: a hp-type Discontinuous Galerkin method

Nicolas Canouet , Loula Fezoui , Serge Piperno

Thème 4 — Simulation et optimisation
de systèmes complexes
Projet Caiman

Rapport de recherche n° 4912 — Août 2003 — 27 pages

Abstract: We present a Discontinuous Galerkin scheme to solve the time-domain Maxwell's equations on conforming or nonconforming orthogonal grids. The method relies on a set of local basis functions whose degree may vary at subgrid interfaces. We also choose a centered mean approximation for the surface integrals and a second-order leap-frog scheme for advancing in time. We prove that the resulting scheme is stable and that it conserves a discrete analog of the electromagnetic energy. We also analyse the dispersion error in the uniform mesh case.

Key-words: electromagnetism, Discontinuous Galerkin, centered fluxes, leap-frog time scheme, L^2 stability, orthogonal nonconforming meshes, PML

Unité de recherche INRIA Sophia Antipolis
2004, route des Lucioles, BP 93, 06902 Sophia Antipolis Cedex (France)
Téléphone : +33 4 92 38 77 77 —Télécopie : +33 4 92 38 77 65

Un schéma Galerkin Discontinu de type hp pour la résolution des équations de Maxwell tridimensionnelles sur des maillages orthogonaux non-conformes

Résumé : On présente ici une nouvelle méthode de Galerkin Discontinue appliquée à la résolution numérique des équations de Maxwell en maillages orthogonaux raffinés de manière conforme ou non-conforme. Le méthode repose sur un jeu de fonctions de base locales dont le degré augmente à l'interface des grilles. Les intégrales de surface sont calculées par une formule centrée. Un schéma saute-mouton est utilisé pour l'intégration temporelle. On est assuré de la stabilité du schéma sur un maillage non-conforme. On montre aussi que la dispersion est très faible sur ce type de maillage

Mots-clés : électromagnétisme, Galerkin discontinu, flux centrés, schéma saute-mouton, stabilité L^2, maillage orthogonal non-conforme, PML

1 Introduction

We are investigating in the present work the solution of the time-domain Maxwell's equations using cartesian grids. When the grid is regular (i.e. all the hexahedra have the same volume), the Finite Difference Time-Domain (**FDTD**) scheme [8] is very efficient. It has good phase property and is easy to implement. It is also very inexpensive as long as the geometry and the physical data (currents, material interfaces, etc..) remain simple. In presence of complex structures, one may still use the Yee's scheme with very fine uniform grids but the solution becomes very costly in time and memory and sometimes impossible to compute. An alternative is to refine the grid only where it is needed and then join the resulting subgrids in a conforming or non-conforming way. It is well known that the increasing of dispersion errors may be the major drawback when applying explicit schemes to locally refined grids. Concerning **FDTD** methods they are few works in the literature and one may cite the space-time mesh refinement approach presented in [4]. The method uses successive refinements of ratio 2 from the coarse to the fine grid and the resulting mesh is non-conforming. One may join the coarse and the fine grids in a conforming way using an irregular subgrid but doing so, **FDTD** schemes can no longer be used. Finite elements or finite volumes become the classical alternatives, see [3] and [5] as examples for each family.
As mentioned above, our goal is to deal with locally refined cartesian grids whether they are conforming or not. We propose in this paper a scheme based on the Discontinuous Galerkin (**DG**) method which has already shown his ability to handle highly distorted grids. One can find a large set of various applications in the review [2] where only few papers concern the Maxwell's equations. On may also cite a previous work [7] which shares with almost all other **DG** schemes the use of some Riemann solver for flux evaluation and a Runge-Kutta scheme for time integration. Generally this results in schemes having good phase properties but are still too diffusive particularly with low order versions. As we know that combining a centered flux approximation with a leap-frog time integration results in a non diffusive scheme, see [5], we select these ingredients to construct new **DG** schemes. Such a method using conforming tetrahedral meshes is described in [6]. The presented work differs from the work cited above in the choice of a new set of basis functions well adapted to cartesian grids as it will be shown in the sequel. Moreover, we propose to increase the degree of the approximation at nonconforming interfaces. It can be viewed as a hp technique used for adaptive computations (p-refinement is the expression used for functional enrichment and h-refinement for mesh refinement). We will also prove that the new scheme is stable, non diffusive (a discrete energy is conserved) and is able to work on highly refined grids without any noticeable dispersion and reflection effects, including for long time calculations.

2 The Discontinuous Galerkin method

We consider in this paper Maxwell's equations in three space dimensions for heterogeneous anisotropic linear media with source $\vec{\mathbf{j}}$ (current density). The electric permittivity tensor $\bar{\bar{\varepsilon}}(x)$ and the magnetic permeability tensor $\bar{\bar{\mu}}(x)$ are varying in space and both symmetric

positive definite (and uniformly bounded). The electric field $\vec{E} = {}^t(E_x, E_y, E_z)$ and the magnetic field $\vec{H} = {}^t(H_x, H_y, H_z)$ verify

$$\begin{cases} \bar{\bar{\varepsilon}}\dfrac{\partial \vec{E}}{\partial t} = \vec{\text{curl}}\, \vec{H} - \vec{\mathbf{j}}, \\ \bar{\bar{\mu}}\dfrac{\partial \vec{H}}{\partial t} = -\vec{\text{curl}}\, \vec{E}. \end{cases} \tag{1}$$

These equations are set and solved on a bounded domain Ω of $\mathbb{R}^3$. On the domain boundary $\partial\Omega$ (of unitary outwards normal $\vec{n}$), a boundary condition is set which is either metallic ($\vec{n} \times \vec{E} = \vec{0}$, on $\partial\Omega_m$) or absorbing ($\vec{n} \times \vec{E} = -c\mu\ \vec{n} \times \left(\vec{n} \times \vec{H}\right)$, on $\partial\Omega_a$, where we assume the medium is isotropic, i.e. $\bar{\bar{\varepsilon}} = \epsilon \mathbb{I}_3$ $\bar{\bar{\mu}} = \mu \mathbb{I}_3$ and the local light speed c is given by $\epsilon\mu c^2 = 1$). We assume we dispose of a partition of the domain Ω into a finite number of orthogonal hexahedra. This partition can be conforming or non-conforming (see figure 1). For each hexahedron $\mathcal{T}_i$, called "finite volume" or "cell", V_i denotes its volume, and $\bar{\bar{\varepsilon}}_i$ and $\bar{\bar{\mu}}_i$ are respectively the local electric permittivity and magnetic permeability tensors of the medium, which could be varying inside the cell $\mathcal{T}_i$. We call interface between two neighbouring finite volumes their intersection (if it is a surface). This interface is a whole face only in the conforming mesh case. For each internal interface $a_{ik} = \mathcal{T}_i \bigcap \mathcal{T}_k$, we denote by $\vec{n}_{ik}$ the integral over the interface of the unitary normal, oriented from $\mathcal{T}_i$ towards $\mathcal{T}_k$. The same definitions are extended to boundary interfaces (in the intersection of the domain boundary $\partial\Omega_m \bigcup \partial\Omega_a$ with a finite volume), the index k corresponding to a fictitious cell outside the domain. We denote by $\vec{\tilde{n}}_{ik} = {}^t(\tilde{n}_{ikx}, \tilde{n}_{iky}, \tilde{n}_{ikz})$ the normalized normals $\vec{\tilde{n}}_{ik} = \vec{n}_{ik}/\|\vec{n}_{ik}\|$. Finally, we denote by $\mathcal{V}_i$ the set of indices of the neighboring finite volumes (i.e. having an interface in common) of the finite volume $\mathcal{T}_i$. We also define the perimeter P_i of $\mathcal{T}_i$ by $P_i = \sum_{k \in \mathcal{V}_i} \|\vec{n}_{ik}\|$.

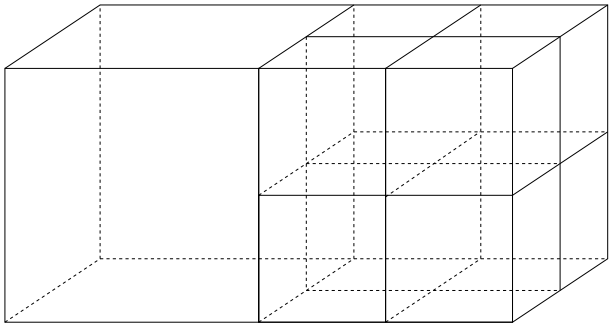

Figure 1: A typical orthogonal non-conforming mesh

2.1 The spatial discretization

Inside each finite volume, the numerical unknowns of the method are related to the orthogonal (in the sense of the classical L^2 scalar product) projection of the electric and magnetic fields on a chosen set of vector basis functions $\vec{\varphi}_{ij}, 1 \leq j \leq d_i$, where d_i denotes the number of local scalar degrees of freedom inside the finite volume $\mathcal{T}_i$. The approximation is allowed to be discontinuous across element boundaries.
Dot-multiplying (1) by a given basis function $\vec{\varphi}_{ij}$, and integrating over $\mathcal{T}_i$ yields

$$\left\{ \begin{array}{l} \displaystyle\int_{\mathcal{T}_i} {}^t\vec{\varphi}_{ij}\bar{\bar{\varepsilon}}_i \frac{\partial \vec{E}}{\partial t} = \int_{\mathcal{T}_i} (\vec{\mathrm{curl}}\, \vec{H} - \vec{\mathbf{j}}).\vec{\varphi}_{ij}, \\ \displaystyle\int_{\mathcal{T}_i} {}^t\vec{\varphi}_{ij}\bar{\bar{\mu}}_i \frac{\partial \vec{H}}{\partial t} = -\int_{\mathcal{T}_i} \vec{\mathrm{curl}}\, \vec{E}.\vec{\varphi}_{ij}. \end{array} \right.$$

Using the identity $\vec{\mathrm{curl}}\, \vec{X}.\vec{\psi} = \vec{\mathrm{curl}}\, \vec{\psi}.\vec{X} - \mathrm{div}(\vec{\psi} \times \vec{X})$, we get

$$\left\{ \begin{array}{l} \displaystyle\int_{\mathcal{T}_i} {}^t\vec{\varphi}_{ij}\bar{\bar{\varepsilon}}_i \frac{\partial \vec{E}}{\partial t} = \int_{\mathcal{T}_i} \vec{\mathrm{curl}}\, \vec{\varphi}_{ij}.\vec{H} - \int_{\partial\mathcal{T}_i} (\vec{\varphi}_{ij} \times \vec{H}).\vec{\tilde{n}} - \int_{\mathcal{T}_i} \vec{\mathbf{j}}.\vec{\varphi}_{ij}, \\ \displaystyle\int_{\mathcal{T}_i} {}^t\vec{\varphi}_{ij}\bar{\bar{\mu}}_i \frac{\partial \vec{H}}{\partial t} = -\int_{\mathcal{T}_i} \vec{\mathrm{curl}}\, \vec{\varphi}_{ij}.\vec{E} + \int_{\partial\mathcal{T}_i} (\vec{\varphi}_{ij} \times \vec{E}).\vec{\tilde{n}}. \end{array} \right. \tag{2}$$

If we denote by $\vec{\mathbf{E}}_i$ and $\vec{\mathbf{H}}_i$ respectively the canonical L^2-orthogonal projections of the fields $\vec{E}$ and $\vec{H}$ on $Span(\vec{\varphi}_{ij},\ 1 \leq j \leq d_i)$ inside the finite volume $\mathcal{T}_i$, verifying the property

$$\forall \vec{\varphi} \in Span(\vec{\varphi}_{ij},\ 1 \leq j \leq d_i), \quad \int_{\mathcal{T}_i} \vec{\mathbf{E}}_i.\vec{\varphi} = \int_{\mathcal{T}_i} \vec{E}.\vec{\varphi}, \quad \int_{\mathcal{T}_i} \vec{\mathbf{H}}_i.\vec{\varphi} = \int_{\mathcal{T}_i} \vec{H}.\vec{\varphi},$$

then, in equations (2), $\vec{\mathbf{E}}_i$ and $\vec{\mathbf{H}}_i$ (and their time-derivative) can be directly used to evaluate volume integrals.

2.2 A centered flux formula

For boundary integrals, since no continuity is imposed on the fields, some additional approximations have to be done. We choose here to use a centered flux approximation:

$$k \in \mathcal{V}_i,\ \forall x \in a_{ik},\ \vec{E}(x) \to \frac{\vec{\mathbf{E}}_i(x) + \vec{\mathbf{E}}_k(x)}{2}, \quad \vec{H}(x) \to \frac{\vec{\mathbf{H}}_i(x) + \vec{\mathbf{H}}_k(x)}{2}.$$

The fields $\vec{\mathbf{E}}_i$ and $\vec{\mathbf{H}}_i$ are then decomposed the following way:

$$\forall x \text{ in } \mathcal{T}_i, \quad \vec{\mathbf{E}}_i(x,t) = \sum_{1 \leq j \leq d_i} E_{ij}(t)\ \vec{\varphi}_{ij}(x), \quad \vec{\mathbf{H}}_i(x,t) = \sum_{1 \leq j \leq d_i} H_{ij}(t)\ \vec{\varphi}_{ij}(x). \tag{3}$$

Inside each control volume, the fields $\vec{\mathbf{E}}_i$ and $\vec{\mathbf{H}}_i$ can now be represented using a chosen number of scalar values E_{il} and H_{il}, for $1 \leq l \leq d_i$. We will denote by $\mathbf{E}_i$ the column $(E_{il})_{1\leq l\leq d_i}$. Finally, this leads to

$$\left\{ \begin{array}{l} \left(M_i^\epsilon \dfrac{\partial \mathbf{E}_i}{\partial t} \right)_j = \displaystyle\int_{\mathcal{T}_i} \vec{\mathrm{curl}}\, \vec{\varphi}_{ij}.\vec{\mathbf{H}}_i - \int_{\mathcal{T}_i} \vec{\mathbf{j}}.\vec{\varphi}_{ij} - \sum_{k\in\mathcal{V}_i} \left(\int_{a_{ik}} (\vec{\varphi}_{ij} \times \frac{\vec{\mathbf{H}}_i + \vec{\mathbf{H}}_k}{2}).\vec{\tilde{n}}_{ik} \right), \\ \left(M_i^\mu \dfrac{\partial \mathbf{H}_i}{\partial t} \right)_j = - \displaystyle\int_{\mathcal{T}_i} \vec{\mathrm{curl}}\, \vec{\varphi}_{ij}.\vec{\mathbf{E}}_i + \sum_{k\in\mathcal{V}_i} \left(\int_{a_{ik}} (\vec{\varphi}_{ij} \times \frac{\vec{\mathbf{E}}_i + \vec{\mathbf{E}}_k}{2}).\vec{\tilde{n}}_{ik} \right), \end{array} \right. \tag{4}$$

where the j subscripts denote the jth component of vectors, the fields $\vec{\mathbf{E}}_i$ and $\vec{\mathbf{H}}_i$ are given in (3) in functions of scalar degrees of freedom, and M_i^ϵ and M_i^μ are square matrices of size d_i, given by

$$\begin{array}{rcl} (M_i^\epsilon)_{jl} & = & \displaystyle\int_{\mathcal{T}_i} {}^t\vec{\varphi}_{ij}\bar{\bar{\varepsilon}}_i\vec{\varphi}_{il},\ 1 \leq j,l \leq d_i, \\ (M_i^\mu)_{jl} & = & \displaystyle\int_{\mathcal{T}_i} {}^t\vec{\varphi}_{ij}\bar{\bar{\mu}}_i\vec{\varphi}_{il},\ 1 \leq j,l \leq d_i. \end{array} \tag{5}$$

It is clear that the matrices M_i^ϵ and M_i^μ are symmetric and definite positive, because the tensors $\bar{\bar{\varepsilon}}_i$ and $\bar{\bar{\mu}}_i$ are symmetric definite positive, and the basis functions $\vec{\varphi}_{ij}$ are assumed to be linearly independent. In the sequel, $\bar{\bar{\varepsilon}}_i$ and $\bar{\bar{\mu}}_i$ are assumed to be constant inside each volume.

2.3 The time discretization

We propose to use a leap-frog time discretization. This kind of time scheme has both advantages to be explicit and to be free of time-dissipation. In the sequel, superscripts refer to time stations and Δt is the fixed time step. The unknowns related to the electric field are approximated at integer time-stations $t^n = n\Delta t$ and are denoted by E_{ij}^n. The unknowns related to the magnetic field are approximated at half-integer time-stations $t^{n+1/2} = (n + 1/2)\Delta t$ and are denoted by $H_{ij}^{n+1/2}$. All definitions for $\mathbf{E}_i^n$, $\mathbf{H}_i^{n+1/2}$, $\vec{\mathbf{E}}_i^n$, and $\vec{\mathbf{H}}_i^{n+1/2}$ are similarly extended. The time scheme directly derives from equation (4) and can be written:

$$\left\{ \begin{array}{l} \left(M_i^\epsilon \dfrac{\mathbf{E}_i^{n+1} - \mathbf{E}_i^n}{\Delta t} \right)_j = \displaystyle\int_{\mathcal{T}_i} \vec{\mathrm{curl}}\, \vec{\varphi}_{ij}.\vec{\mathbf{H}}_i^{n+1/2} - \int_{\mathcal{T}_i} \vec{\mathbf{j}}.\vec{\varphi}_{ij} - \sum_{k\in\mathcal{V}_i} \int_{a_{ik}} (\vec{\varphi}_{ij} \times \frac{\vec{\mathbf{H}}_i^{n+1/2} + \vec{\mathbf{H}}_k^{n+1/2}}{2}).\vec{\tilde{n}}_{ik}, \\ \left(M_i^\mu \dfrac{\mathbf{H}_i^{n+3/2} - \mathbf{H}_i^{n+1/2}}{\Delta t} \right)_j = - \displaystyle\int_{\mathcal{T}_i} \vec{\mathrm{curl}}\, \vec{\varphi}_{ij}.\vec{\mathbf{E}}_i^{n+1} + \sum_{k\in\mathcal{V}_i} \int_{a_{ik}} (\vec{\varphi}_{ij} \times \frac{\vec{\mathbf{E}}_i^{n+1} + \vec{\mathbf{E}}_k^{n+1}}{2}).\vec{\tilde{n}}_{ik}. \end{array} \right. \tag{6}$$

2.4 Treatment of boundary conditions

The metallic and absorbing conditions are dealt with in weak sense by taking some values for the fields $\vec{\mathbf{E}}$ and $\vec{\mathbf{H}}$ inside the fictitious finite volume beyond the boundary face. In the two

cases, a_{ik} denotes a boundary face between a boundary cell $\mathcal{T}_i$ and its fictitious neighbour $\mathcal{T}_k$.
For a metallic boundary face a_{ik}, we use

$$\text{METALLIC BOUNDARY:} \quad \forall x \in a_{ik},\ \vec{\mathbf{E}}_k^n(x) = -\vec{\mathbf{E}}_i^n(x),\ \vec{\mathbf{H}}_k^{n+1/2}(x) = \vec{\mathbf{H}}_i^{n+1/2}(x). \tag{7}$$

A first-order Silver–Müller absorbing condition is used on the absorbing boundary $\partial\Omega_a$. Let us recall that the medium is assumed to be isotropic near the absorbing boundary $\partial\Omega_a$ then the permeability and permittivity tensors $\bar{\bar{\varepsilon}}$ and $\bar{\bar{\mu}}$ are scalars. Using the wave speed $c = 1/\sqrt{\mu\epsilon}$, the Silver–Müller absorbing condition can be written

$$\vec{\tilde{n}} \times E = -c\mu\ \vec{\tilde{n}} \times \left(\vec{\tilde{n}} \times H\right), \qquad \vec{\tilde{n}} \times H = c\epsilon\ \vec{\tilde{n}} \times \left(\vec{\tilde{n}} \times E\right),$$

where $\vec{\tilde{n}}$ is the outgoing unitary normal. This boundary condition is exact for outgoing plane waves (with a wave vector collinear with $\vec{\tilde{n}}$). This condition is a first-order approximation, asymptotically correct when the fictitious absorbing boundary is far enough.
In view of the absorbing boundary condition above, we propose the following fictitious fields $\vec{\mathbf{H}}_k^{n+1/2}$ and $\vec{\mathbf{E}}_k^{n+1}$ over an absorbing interface a_{ik} between the real finite volume $\mathcal{T}_i$ and its fictitious neighbor $\mathcal{T}_k$ (these fields are used in the scheme (6)) for the absorbing interface a_{ik}):

$$\text{ABSORBING BOUNDARY:} \quad \forall x \in a_{ik},\ \left\{ \begin{array}{l} \vec{\mathbf{H}}_k^{n+1/2}(x) = c_i\epsilon_i\ \vec{\tilde{n}}_{ik} \times \vec{\mathbf{E}}_i^n(x), \\ \vec{\mathbf{E}}_k^{n+1}(x) = -c_i\mu_i\ \vec{\tilde{n}}_{ik} \times \vec{\mathbf{H}}_i^{n+1/2}(x), \end{array} \right. \tag{8}$$

where $c_i = 1/\sqrt{\mu_i\epsilon_i}$ is the local wave speed (recall the medium is assumed isotropic near the absorbing boundary).

2.5 Perfectly Matched Layer Absorbing Medium

To deal efficiently with the solution of electromagnetic problems in unbounded regions, we study the application of the Perfectly Matched Layer (PML) introduced by Berenger [1]. Let us recall that this method is based on a split-field formulation of Maxwell's equations. Each vector field component is split into two orthogonal components. We rewrite the 12 PML equations in the following way :

$$\left\{ \begin{array}{l} \bar{\bar{\varepsilon}}\dfrac{\partial \vec{E_1}}{\partial t} + S_1(\vec{\sigma})\vec{E_1} = \vec{r_1}(\vec{H_1} + \vec{H_2}), \\ \bar{\bar{\varepsilon}}\dfrac{\partial \vec{E_2}}{\partial t} + S_2(\vec{\sigma})\vec{E_2} = \vec{r_2}(\vec{H_1} + \vec{H_2}), \\ \bar{\bar{\mu}}\dfrac{\partial \vec{H_1}}{\partial t} + S_1(\vec{\sigma}^*)\vec{H_1} = -\vec{r_1}(\vec{E_1} + \vec{E_2}), \\ \bar{\bar{\mu}}\dfrac{\partial \vec{H_2}}{\partial t} + S_2(\vec{\sigma}^*)\vec{H_2} = -\vec{r_2}(\vec{E_1} + \vec{E_2}), \end{array} \right. \tag{9}$$

where $\vec{E_1} = {}^t(E_{xy}, E_{yz}, E_{zx})$, $\vec{E_2} = {}^t(E_{xz}, E_{yx}, E_{zy})$, $\vec{H_1} = {}^t(H_{xy}, H_{yz}, H_{zx})$ and $\vec{H_2} = {}^t(H_{xz}, H_{yx}, H_{zy})$. The operators S_1 and S_2 are given by :

$$S_1(\vec{v}) = \begin{pmatrix} v_y & 0 & \\ 0 & v_z & 0 \\ 0 & 0 & v_x \end{pmatrix} \text{ and } S_2(\vec{v}) = \begin{pmatrix} v_z & 0 & \\ 0 & v_x & 0 \\ 0 & 0 & v_y \end{pmatrix}. \tag{10}$$

The differential operators $\vec{r}_1$ and $\vec{r}_2$ are defined by

$$\vec{r}_1 = \begin{pmatrix} 0 & 0 & \partial_y \\ \partial_z & 0 & 0 \\ 0 & \partial_x & 0 \end{pmatrix} \text{ and } \vec{r}_2 = \begin{pmatrix} 0 & -\partial_z & 0 \\ 0 & 0 & -\partial_x \\ -\partial_y & 0 & 0 \end{pmatrix}. \tag{11}$$

Following the section 2.1, we dot-multiply (9) by a basis function $\vec{\varphi}_{ij}$ and we integrate over $\mathcal{T}_i$:

$$\left\{ \begin{array}{l} \displaystyle\int_{\mathcal{T}_i} {}^t\vec{\varphi}_{ij}\bar{\bar{\varepsilon}}_i(\frac{\partial \vec{E_1}}{\partial t} + S_1(\vec{\sigma})\vec{E_1}) = \int_{\mathcal{T}_i} (\vec{r_1}(\vec{H_1} + \vec{H_2})).\vec{\varphi}_{ij}, \\ \displaystyle\int_{\mathcal{T}_i} {}^t\vec{\varphi}_{ij}\bar{\bar{\varepsilon}}_i(\frac{\partial \vec{E_2}}{\partial t} + S_2(\vec{\sigma})\vec{E_2}) = \int_{\mathcal{T}_i} (\vec{r_2}(\vec{H_1} + \vec{H_2})).\vec{\varphi}_{ij}, \\ \displaystyle\int_{\mathcal{T}_i} {}^t\vec{\varphi}_{ij}\bar{\bar{\mu}}_i(\frac{\partial \vec{H_1}}{\partial t} + S_1(\vec{\sigma}^*)\vec{H_1}) = -\int_{\mathcal{T}_i} (\vec{r_1}(\vec{E_1} + \vec{E_2})).\vec{\varphi}_{ij}, \\ \displaystyle\int_{\mathcal{T}_i} {}^t\vec{\varphi}_{ij}\bar{\bar{\mu}}_i(\frac{\partial \vec{H_2}}{\partial t} + S_2(\vec{\sigma}^*)\vec{H_2}) = -\int_{\mathcal{T}_i} (\vec{r_2}(\vec{E_1} + \vec{E_2})).\vec{\varphi}_{ij}. \end{array} \right. \tag{12}$$

Integrating by part, we can write

$$\left\{ \begin{array}{l} \displaystyle\int_{\mathcal{T}_i} {}^t\vec{\varphi}_{ij}\bar{\bar{\varepsilon}}_i(\frac{\partial \vec{E_1}}{\partial t} + S_1(\vec{\sigma})\vec{E_1}) = \int_{\mathcal{T}_i} \vec{r_1}(\vec{\varphi}_{ij}).(\vec{H_1} + \vec{H_2}) - \int_{\partial\mathcal{T}_i} S_1(\vec{n})\vec{\varphi}_{ij}.(\vec{H_1} + \vec{H_2}), \\ \displaystyle\int_{\mathcal{T}_i} {}^t\vec{\varphi}_{ij}\bar{\bar{\varepsilon}}_i(\frac{\partial \vec{E_2}}{\partial t} + S_2(\vec{\sigma})\vec{E_2}) = \int_{\mathcal{T}_i} \vec{r_2}(\vec{\varphi}_{ij}).(\vec{H_1} + \vec{H_2}) - \int_{\partial\mathcal{T}_i} S_2(\vec{n})\vec{\varphi}_{ij}.(\vec{H_1} + \vec{H_2}), \\ \displaystyle\int_{\mathcal{T}_i} {}^t\vec{\varphi}_{ij}\bar{\bar{\mu}}_i(\frac{\partial \vec{H_1}}{\partial t} + S_1(\vec{\sigma}^*)\vec{H_1}) = -\int_{\mathcal{T}_i} \vec{r_1}(\vec{\varphi}_{ij}).(\vec{E_1} + \vec{E_2}) + \int_{\partial\mathcal{T}_i} S_1(\vec{n})\vec{\varphi}_{ij}.(\vec{E_1} + \vec{E_2}), \\ \displaystyle\int_{\mathcal{T}_i} {}^t\vec{\varphi}_{ij}\bar{\bar{\mu}}_i(\frac{\partial \vec{H_2}}{\partial t} + S_2(\vec{\sigma}^*)\vec{H_2}) = -\int_{\mathcal{T}_i} \vec{r_2}(\vec{\varphi}_{ij}).(\vec{E_1} + \vec{E_2}) + \int_{\partial\mathcal{T}_i} S_2(\vec{n})\vec{\varphi}_{ij}.(\vec{E_1} + \vec{E_2}). \end{array} \right. \tag{13}$$

To discretize $\vec{E_1}$, $\vec{E_2}$, $\vec{H_1}$ and $\vec{H_2}$, we use the same basis functions as for $\vec{E}$ and $\vec{H}$. Boundary integrals are also evaluated with a centered flux formula and an exponential scheme is used for the time integration.

Now the absorbing medium itself has to be bounded. Using a metallic boundary condition on the reconstructed fields $\vec{H_1}+\vec{H_2}$ and $\vec{E_1}+\vec{E_2}$ leads in some cases to numerical instabilities. Thus we propose to use the first order boundary absorbing condition (8) which makes the scheme stable.

3 Stability analysis

We recall here a stability result given in [6] for arbitrary polyhedra grids. However the proof does not use neither the way the polyhedra are connected or the exact particular form of the basis functions, thus this result is still true for the **DG** method described here. It has shown in [6] that for a class of **DG** schemes supplemented by a metallic boundary, a discrete electromagnetic energy is exactly conserved which proves that the scheme is non-diffusive. Moreover, under some CFL condition on Δt, this energy is a positive definite quadratic form of the numerical unknowns $\mathbf{H}_i^{n-1/2}$ and $\mathbf{E}_i^n$ ensuring the stability of the scheme. The discrete energy has the following definition.

Definition 3.1 *For a finite volume partition $\mathcal{G}$ of the domain Ω with metallic boundary conditions ($\partial\Omega = \partial\Omega_m$), we consider the following electromagnetic energy inside each finite volume and in the whole domain:*

$$(i)\ \forall i,\ \mathbb{E}_i^n = \frac{1}{2}\int_{\mathcal{T}_i} \left({}^t\vec{\mathbf{E}}_i^n \bar{\bar{\varepsilon}}_i \vec{\mathbf{E}}_i^n + {}^t\vec{\mathbf{H}}_i^{n-1/2} \bar{\bar{\mu}}_i \vec{\mathbf{H}}_i^{n+1/2} \right) = \frac{1}{2}\left({}^t\mathbf{E}_i^n M_i^\epsilon \mathbf{E}_i^n + {}^t\mathbf{H}_i^{n-1/2} M_i^\mu \mathbf{H}_i^{n+1/2} \right),$$

$$(ii)\ \mathbb{E}^n = \sum_{i\in\mathcal{G}} \mathbb{E}_i^n .$$

where the matrices M^μ and M^ϵ are given by (5).

4 Basis Functions

We introduce a set of basis functions well adapted to cartesian grids. A classical approach is to use a basis of $\mathbb{P}^n$ (polynomial of degree n). We propose basis functions which are less costly and which ensure the divergence conservation in a strong way.
Let us consider a finite number of orthogonal hexahedra. For each hexahedron $\mathcal{T}_i$, we denote by $\mathbf{G_i} = {}^t(x_{Gi}, y_{Gi}, z_{Gi})$ its mass center and $\mathbf{\Delta} = {}^t(\Delta x_i, \Delta y_i, \Delta z_i)$ its size. We introduce the space $\mathbb{P}^1_{div}$ generated by the following basis functions :

$$\left\{ \begin{array}{lll} \vec{\varphi}_{i1} = {}^t(1,0,0), & \vec{\varphi}_{i2} = {}^t(y - y_{Gi}, 0, 0), & \vec{\varphi}_{i3} = {}^t(z - z_{Gi}, 0, 0), \\ \vec{\varphi}_{i4} = {}^t(0,1,0), & \vec{\varphi}_{i5} = {}^t(0, x - x_{Gi}, 0), & \vec{\varphi}_{i6} = {}^t(0, z - z_{Gi}, 0), \\ \vec{\varphi}_{i7} = {}^t(0,0,1), & \vec{\varphi}_{i8} = {}^t(0, 0, x - x_{Gi}), & \vec{\varphi}_{i9} = {}^t(0, 0, y - y_{Gi}). \end{array} \right. \tag{14}$$

The scheme given by (6)-(14) will be named **DG**-$\mathbb{P}^1_{div}$.
In the non-conforming case, a higher approximation is required. We introduce the space $\mathbb{P}^2_{div}$ where $\mathbb{P}^2_{div} \backslash \mathbb{P}^1_{div}$ is generated by :

$$\left\{ \begin{array}{ll} \vec{\varphi}_{i10} = {}^t((y - y_{Gi})(z - z_{Gi}), 0, 0), & \vec{\varphi}_{i11} = {}^t((y - y_{Gi})^2 - \Delta y_i^2/12, 0, 0), \\ \vec{\varphi}_{i12} = {}^t((z - z_{Gi})^2 - \Delta z_i^2/12, 0, 0), & \vec{\varphi}_{i13} = {}^t(0, (x - x_{Gi})(z - z_{Gi}), 0), \\ \vec{\varphi}_{i14} = {}^t(0, (x - x_{Gi})^2 - \Delta x_i^2/12, 0), & \vec{\varphi}_{i15} = {}^t(0, (z - z_{Gi})^2 - \Delta z_i^2/12, 0), \\ \vec{\varphi}_{i16} = {}^t(0, 0, (x - x_{Gi})(y - y_{Gi})), & \vec{\varphi}_{i17} = {}^t(0, 0, (x - x_{Gi})^2 - \Delta x_i^2/12), \\ \vec{\varphi}_{i18} = {}^t(0, 0, (y - y_{Gi})^2 - \Delta y_i^2/12). & \end{array} \right. \tag{15}$$

Remark 4.1 *Let us note that using piecewise constant functions as a basis ($\mathbb{P}_0$), will result in a centered finite volume scheme which was already presented in [5]*

Remark 4.2 *The basis of $\mathbb{P}^n_{div}$ $(n = 1, 2)$ are orthogonal with respect to the L^2 scalar product. As a result the scheme will not even require the inversion of the local 9×9 mass matrix. Another advantage is that the orthogonal basis makes the hybrid scheme $\mathbb{P}^1_{div}/\mathbb{P}^2_{div}$ easy to implement.*

The spaces $\mathbb{P}^n_{div}$ $(n = 1, 2)$ require a smaller number of degrees of freedom than the spaces $\mathbb{P}^n$ (table 1). However, the spaces $\mathbb{P}^n_{div}$ seems to be well adapted to solve Maxwell equations. Indeed, if we denote by $\vec{\mathbf{H}}_{\mathbb{P}^1}$ and $\vec{\mathbf{H}}_{\mathbb{P}^1_{div}}$ the L^2-orthogonal projections of the fields $\vec{H}$ on respectively the spaces $\mathbb{P}^1$ and $\mathbb{P}^1_{div}$, we have on each hexahedron $\mathcal{T}_i$

$$\vec{\text{curl}}\, \vec{\mathbf{H}}_{\mathbb{P}^1_{div},i} = \vec{\text{curl}}\, \vec{\mathbf{H}}_{\mathbb{P}^1,i}. \tag{16}$$

Scheme	$\mathbb{P}^0$	$\mathbb{P}^1_{div}$	$\mathbb{P}^1$	$\mathbb{P}^2_{div}$	$\mathbb{P}^2$
Degrees of freedom	3	9	12	18	30

Table 1: Number of degrees of freedom for one field

Moreover, it is easy to check that :

$$\begin{cases} \dfrac{\partial}{\partial x}\vec{\mathbf{H}}_{\mathbb{P}^n_{div},i}.{}^t(1,0,0) = 0, \\ \dfrac{\partial}{\partial y}\vec{\mathbf{H}}_{\mathbb{P}^n_{div},i}.{}^t(0,1,0) = 0, \\ \dfrac{\partial}{\partial z}\vec{\mathbf{H}}_{\mathbb{P}^n_{div},i}.{}^t(0,0,1) = 0. \end{cases} \tag{17}$$

It is a strong way to ensure the Gauss'law on each finite volume $\mathcal{T}_i$:

$$\text{div}(\bar{\bar{\mu}}_i \vec{\mathbf{H}}_{\mathbb{P}^n_{div},i}) = 0. \tag{18}$$

Since our formulation is symmetric for both fields we have the same relation for the field $\vec{E}$ which writes on each finite finite volume $\mathcal{T}_i$:

$$\text{div}(\bar{\bar{\varepsilon}}_i \vec{\mathbf{E}}_{\mathbb{P}^n_{div},i}) = 0. \tag{19}$$

That is to say the volumic charge density is equal to zero on each hexahedron $\mathcal{T}_i$. Our model can not create volumic charges. Nevertheless, surfacic charges are allowed because the fields are discontinuous on each interface a_{ik} :

$$\rho_{a_{ik}} = \vec{n}_{ik}.(\vec{\mathbf{E}}_{\mathbb{P}^n_{div},k} - \vec{\mathbf{E}}_{\mathbb{P}^n_{div},i}). \tag{20}$$

We give in the table 2 the value of $\nu = \Delta t\sqrt{\Delta x^{-2} + \Delta y^{-2} + \Delta z^{-2}}$ used for the Discontinuous Galerkin method compared to its value for the Yee's scheme [8]. These values are obtained numerically in the case $\Delta x = \Delta y = \Delta z$.

	Yee	$\mathbb{P}^0$	$\mathbb{P}^1_{div}$	$\mathbb{P}^2_{div}$
ν	1	2	0.65	0.4

Table 2: Stability condition

5 Dispersion Analysis

In this section we study the phase error of the **DG**-$\mathbb{P}^1_{div}$ scheme on cubic meshes and compare it to the Yee's scheme as a reference scheme on orthogonal grids. We will restrict the study to plane waves which propagate in one of the principal directions given by the vector $\mathbf{k} =^t (1,0,0)$, or $^t(1,1,0)$ or $^t(1,1,1)$ and details will be given for the first direction. Let us note that this restriction is due to the difficulty in evaluating the eigenvalues of a 18×18 matrix even with the help of formal mathematical softwares.
When $\mathbf{k} =^t (1,0,0)$ the problem reduces to a one-dimensional system and the unknowns are the components H_y and E_z with 2 degrees of freedom for each one. Let us assume a uniform grid (Δx constant) and set $\mathbf{V}_j =^t (H_{j,1}, H_{j,2}, E_{j,1}, E_{j,2})$ a plane wave on the cell $[j\Delta x, (j+1)\Delta x]$, the indices y and z being omitted for H and E respectively.
As a plane wave, $\mathbf{V}_j$ writes $\mathbf{A}_j \exp(i\omega(n+s)\Delta t + ijk\Delta x)$ where $\mathbf{A}_j$ is the amplitude vector, $i = \sqrt{-1}$,$k = |\mathbf{k}|$, $s = 0$ for the electric components and $s = \frac{1}{2}$ for magnetic ones.
By injecting the plane wave $\mathbf{V}_j$ on the **DG**-$\mathbb{P}^1_{div}$ scheme we obtain the following system:

$$\frac{2i}{\Delta t}\sin\left(\frac{\omega\Delta t}{2}\right)\begin{pmatrix} \mu_j & 0 & 0 & 0 \\ 0 & \mu_j & 0 & 0 \\ 0 & 0 & \varepsilon_j & 0 \\ 0 & 0 & 0 & \varepsilon_j \end{pmatrix}\mathbf{V}_j = P\mathbf{V}_j, \tag{21}$$

with

$$P = \begin{pmatrix} 0 & 0 & s & t \\ 0 & 0 & u & v \\ s & t & 0 & 0 \\ u & v & 0 & 0 \end{pmatrix},$$

$$\begin{cases} s = \dfrac{i\sin(k\Delta x)}{\Delta x}, & t = (1 - cos(k\Delta x)), \\ u = \dfrac{3}{\Delta x^2}(2cos(k\Delta x) - 2), & v = \dfrac{-3i\sin(k\Delta x)}{\Delta x}. \end{cases}$$

We calculate the eigenvalues of the matrix P using Taylor series expansion:

$$\begin{array}{l} \lambda_1/k = 1 + k^2\Delta x^2/48 + O(k^4\Delta x^4), \\ \lambda_2/k = -1 - k^2\Delta x^2/48 + O(k^4\Delta x^4), \\ \lambda_3/k = 3 + 5k^2\Delta x^2/16 + O(k^4\Delta x^4), \\ \lambda_4/k = -3 - 5k^2\Delta x^2/16 + O(k^4\Delta x^4). \end{array} \tag{22}$$

Using the first two eigenvalues we obtain the following dispersive relation:

$$\omega^2 = k^2c^2\left(1 + k^2\Delta x^2\left(\frac{\nu^2}{36} + \frac{1}{24}\right) + O(k^4\Delta x^4)\right). \tag{23}$$

where $\nu = c\Delta t/\Delta x$. Let us note that the eigenvectors corresponding to λ_3 and λ_4 tend to ${}^t(0, \pm i, 0, \pm 1)$ when Δx tends to zero thus they are considered as spurious modes.
The same calculations driven for the two other directions of vector $\mathbf{k}$ lead to the following dispersive relations:

$$\begin{array}{ll} \mathbf{k} = |k|\ {}^t(1,1,0): & \omega^2 = |k|^2c^2\left(1 + |k|^2\Delta x^2\left(\frac{\nu^2}{36} - \frac{1}{168}\right) + O(|k|^4\Delta x^4)\right), \\ \mathbf{k} = |k|\ {}^t(1,1,1): & \omega^2 = |k|^2c^2\left(1 + |k|^2\Delta x^2\left(\frac{\nu^2}{36} - \frac{1}{36}\right) + O(|k|^4\Delta x^4)\right). \end{array} \tag{24}$$

We recall the corresponding dispersive relations of the Yee's scheme:

$$\begin{array}{ll} \mathbf{k} = |k|\ {}^t(1,0,0): & \omega^2 = |k|^2c^2\left(1 + |k|^2\Delta x^2\left(\frac{\nu^2}{36} - \frac{1}{12}\right) + O(|k|^4\Delta x^4)\right), \\ \mathbf{k} = |k|\ {}^t(1,1,0): & \omega^2 = |k|^2c^2\left(1 + |k|^2\Delta x^2\left(\frac{\nu^2}{36} - \frac{1}{24}\right) + O(|k|^4\Delta x^4)\right), \\ \mathbf{k} = |k|\ {}^t(1,1,1): & \omega^2 = |k|^2c^2\left(1 + |k|^2\Delta x^2\left(\frac{\nu^2}{36} - \frac{1}{36}\right) + O(|k|^4\Delta x^4)\right). \end{array} \tag{25}$$

The figures 2 and 3 show the second order term of the dispersion error of **DG**-$\mathbb{P}^1_{div}$ and Yee's scheme as a function of the Courant number ν which is in $[0, 0.65]$ for the first and $[0, 1]$ for the second scheme respectively. The results are normalized using the maximum error Yee's scheme has when $\mathbf{k} = |k|\ {}^t(1,0,0)$ and $\nu = 0$.
Although this study is not as complete as with an arbitrary propagation direction $\mathbf{k}$ we consider that the three directions we have chosen allow us to draw some conclusions. From figures 2 et 3, one may retain that:

1. When ν is maximum (in the limit of the stability of each scheme), the dispersion errors of both scheme are comparable with a maximum of 0.67 for Yee and 0.64 for the **DG** scheme.

2. When ν is small, this maximum increases for the Yee's scheme while it is reduced for our scheme which means that using small time steps will not damage its precision. Thus one may conclude that we can still use the **DG**-$\mathbb{P}^1_{div}$ with refined grids without any local time stepping as it is the case for the Yee's scheme.

The table 3 shows different minima and maxima of the dispersion errors for the two schemes.

	Maximum Error		Minimum Error	
	GD-$\mathbb{P}^1_{div}$	Yee	GD-$\mathbb{P}^1_{div}$	Yee
ν_{max}	0.64	0.67	0.07	0
$\nu_{max}/2$	0.53	0.91	0.04	0.25
$\nu_{max}/4$	0.51	0.98	0.06	0.31
0	0.5	1	0.07	0.33

Table 3: Maxima and Minima of the dispersion error for different values of ν

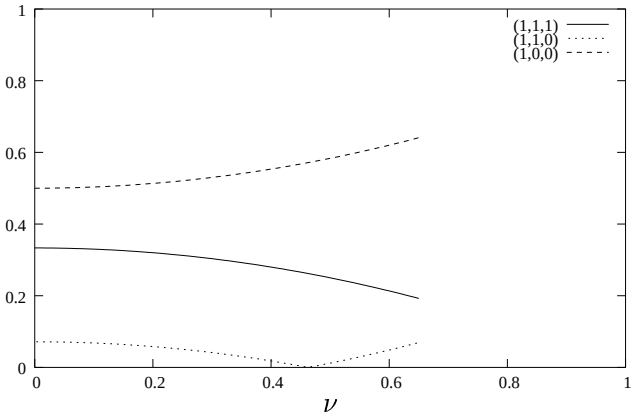

Figure 2: **DG**-$\mathbb{P}^1_{div}$: 2nd order term of the dispersion error as function of ν for various $\mathbf{k}$

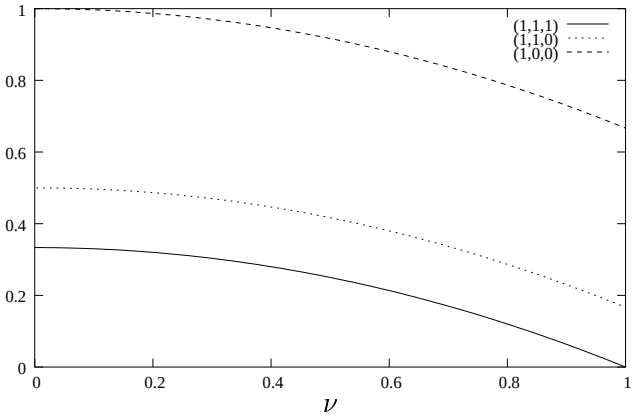

Figure 3: Yee : 2nd order term of the dispersion error as function of ν for various $\mathbf{k}$

We propose now to compare the phase error of the two schemes on refined grids. We consider a domain composed of two adjacent cubic grids with space steps noted Δx_{max} for the fine grid and Δx_{min} for the coarse one and set $n = \Delta x_{max}/\Delta x_{min}$.
We choose a propagation direction parallel to ${}^t(1,0,0)$ axis and write the dispersion relation for both schemes as a function of Δx_{min} :

1. **DG**-$\mathbb{P}^1_{div}$ scheme with $\nu = 0.65$

   - Fine grid :

   $$\omega^2 = |k|^2 c^2 \left(1 + |k|^2 \Delta x_{min}^2 \left(\frac{\nu^2}{36} + \frac{1}{24}\right) + O(|k|^4 \Delta x^4)\right),$$

   - Coarse grid :

   $$\omega^2 = |k|^2 c^2 \left(1 + |k|^2 \Delta x_{min}^2 n^2 \left(\frac{\nu^2}{36n^2} + \frac{1}{24}\right) + O(|k|^4 \Delta x^4)\right).$$

2. Yee's scheme with $\nu = 1$

   - Fine grid :

   $$\omega^2 = |k|^2 c^2 \left(1 + |k|^2 \Delta x_{min}^2 \left(\frac{\nu^2}{36} - \frac{1}{12}\right) + O(|k|^4 \Delta x^4)\right),$$

   - Coarse grid with a uniform time step :

   $$\omega^2 = |k|^2 c^2 \left(1 + |k|^2 \Delta x_{min}^2 n^2 \left(\frac{\nu^2}{36n^2} - \frac{1}{12}\right) + O(|k|^4 \Delta x^4)\right),$$

- Coarse grid with a local time step :

$$\omega^2 = |k|^2 c^2 \left(1 + |k|^2 \Delta x_{min}^2 n^2 \left(\frac{\nu^2}{36} - \frac{1}{12}\right) + O(|k|^4 \Delta x^4)\right).$$

The same study is done with the propagation directions ${}^t(1,1,0)$ and ${}^t(1,1,1)$. Second order terms of the dispersion error are reported on tables 4, 5 and 6 for two values of the refinement rate ($n = 4$ and $n = 10$). We use the same normalization as table 3 based on Δx_{min} in the both fine and coarse grids (i.e. we give $(\omega^2 - |k|^2 c^2)/(|k|^4 c^2 \Delta x_{min}/12)$). Therefore, a term n^2 appears in the second order error term on the coarse grid. This is the reason why it is larger than the fine grid one. We indicate that the Yee's scheme results with a local time step are computed using the optimal value $\nu = 1$. One may retain from these results the following :

1. In the directions ${}^t(1,1,0)$ and ${}^t(1,0,0)$, the **DG**-$\mathbb{P}^1_{div}$ scheme is less dispersive than Yee's scheme with a local time step.

2. The comparison is clearly in favor of the Yee's scheme in the direction ${}^t(1,1,1)$. We must note however that the results corresponding to the local time step case were obtained using the optimal value $\nu = 1$ (which eliminates the second order term of the dispersion relation in the direction ${}^t(1,1,1)$) which is not always possible in practice. Thus, it was reported in [4] for example that the CFL number has to be reduced significantly as soon as the refinement rate exceeded the value 2. At the allowed values of ν, the dispersion error of the Yee's scheme becomes comparable to the **DG**-$\mathbb{P}^1_{div}$'s one.

	DG-$\mathbb{P}^1_{div}$	Yee with no local time step	Yee with local time step
Fine grid	0.64	0.67	0.67
Coarse grid (refinement rate 1:4)	8,1	15,6	10,6
Coarse grid (refinement rate 1:10)	50,1	99,7	66,7

Table 4: Direction ${}^t(1,0,0)$: 2nd order term of dispersion error

	DG-$\mathbb{P}^1_{div}$	Yee with no local time step	Yee with local time step
Fine grid	0.07	0.16	0.16
Coarse grid (refinement rate 1:4)	1	7.6	2.67
Coarse grid (refinement rate 1:10)	7	49.6	16.7

Table 5: Direction ${}^t(1,1,0)$: 2nd order term of dispersion error

	DG-$\mathbb{P}^1_{div}$	Yee with no local time step	Yee with local time step
Fine grid	0.19	0	0
Coarse grid (refinement rate 1:4)	5.2	5	0
Coarse grid (refinement rate 1:10)	33.2	33	0

Table 6: Direction ${}^t(1,1,1)$: 2nd order term of dispersion error

6 How to deal with non-conforming grids ?

Using $\mathbb{P}^1_{div}$ approximation with a conforming mesh refinement is very efficient. Unfortunately, this discretization is not able to handle non-conforming grids since many reflections occur at subgrid interfaces and damage the solution. An alternative is to increase the order of the approximation using $\mathbb{P}^2_{div}$ for example. However, this approach will require a larger number of degrees of freedom which will raise the CPU time and memory costs. We propose to use $\mathbb{P}^1_{div}$ approximation in each volume except when this volume is inside the coarse subgrid but has at least one face on the fine subgrid, see figure 4. In these volumes we use a $\mathbb{P}^2_{div}$ approximation. We name the resulting scheme $\mathbb{P}^1_{div}/\mathbb{P}^2_{div}$. We have observed numerically that the stability condition is still given by $\nu \leq 0.65$ which is surprising since a smaller bound is expected when increasing the degree of polynomials.

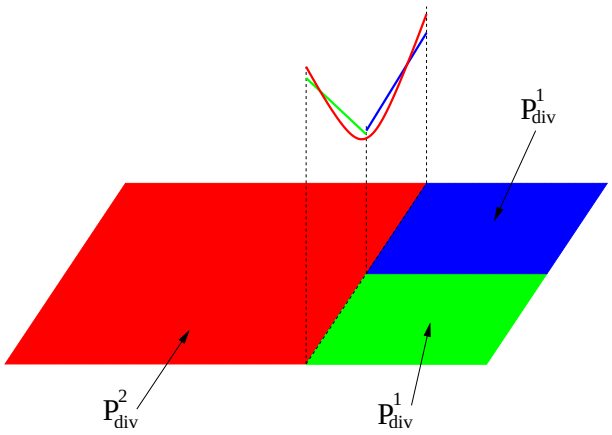

Figure 4: $\mathbb{P}^1_{div}/\mathbb{P}^2_{div}$: 2D non-conforming example

7 Numerical Results

We present some numerical results to validate our method in various configurations. Fist we want to test the ability of the **DG** method in long time simulations which point out the phase errors. Thus we select the evolution of an eigenmode in a cube with non-conforming mesh discretizations. We compare the computed solution to the analytic one and verify that the discrete electromagnetic energy is conserved.
The second test case deals with the use and efficiency of the PML method in the version presented above. A radiating dipole in the vacuum is simulated using uniform and non-conforming refined grids.
The last case is more complex since it concerns the propagation of a gaussian incident wave in a metallic shelter with a small aperture.

7.1 Resonant cavity

We compute the $(1, 1, 1)$ mode which is a standing wave of 0.260 GHz frequency in a cube of 1 m of side. The central zone of the cavity is refined in a non-conforming way. The degrees of freedom are initialized by the projection of the exact solution on the local basis functions. The discretization used for the coarse grid is 15 points per wavelength. The rate between the two grids is 10. Thus, the discretization of the fine grid is 150 points per wavelength. We stop the simulation after 45 periods.
We plot on figure 5 the time evolution at a point of the coarse grid of the field E_z on the last 5 periods compared to the exact solution. There is no dispersion whereas the refinement rate is very high and the simulation is long. The figure 6 shows the discrete energy time evolution in the whole cavity. As expected, there is no diffusion. We plot on figure 7 the solution at the end of the computation projected on the coarse grid. One can see that computed and

exact solutions compare very well.
These results are very good and show that the dispersion of the method is very small although the refinement rate is high.

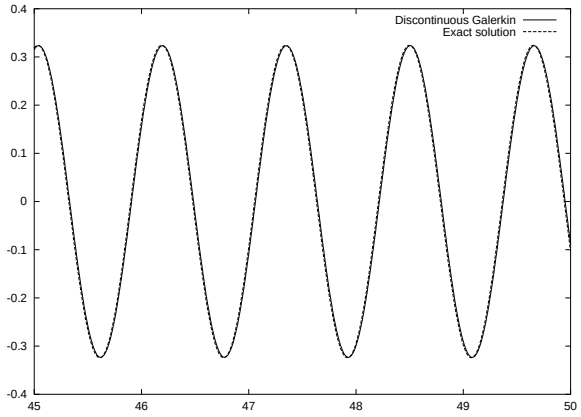

Figure 5: Field E_z : time evolution / Zoom on the last 5 periods / Refinement rate : 10

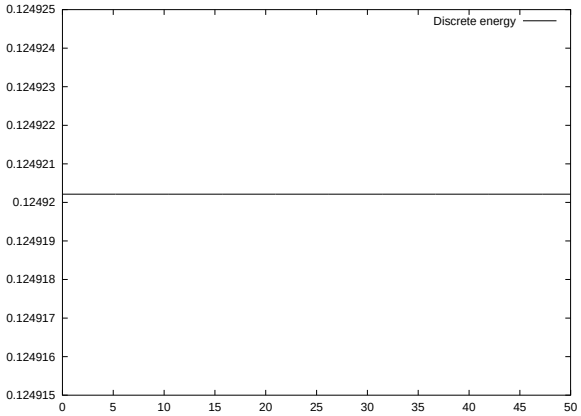

Figure 6: Discrete energy

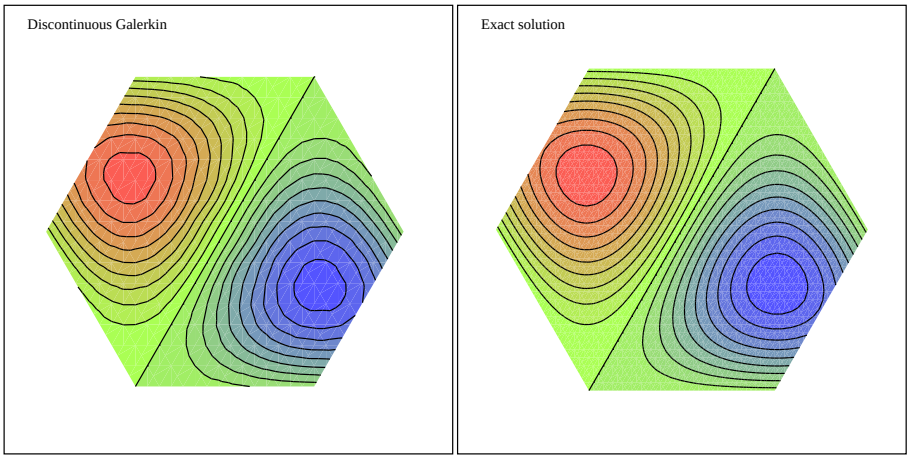

Figure 7: Approximate and exact E_z fields (plane cut $x + y + z = 3/2$)

7.2 Radiating dipole

We compute a dipole located in some hexahedron $\mathcal{T}_i$ collinear with the z axis : $\vec{\mathbf{j}} = {}^t(0, 0, \mathbf{j}_z)$ using the relation

$$\int_{\mathcal{T}_i} \mathbf{j}_z = \frac{\partial \rho}{\partial t},$$

and we choose the following gaussian pulse:

$$\rho(t) = 10^{-10} exp\left(-\left(\frac{t - 3T}{T}\right)^2\right), \ (T = 2ns).$$

Assuming $\vec{\mathbf{j}}$ constant in $\mathcal{T}_i$, it's easy to check that

$$\begin{cases} \int_{\mathcal{T}_i} \vec{\mathbf{j}}.\vec{\varphi}_{ij} = 0, \ \forall j \neq 7, \\ \int_{\mathcal{T}_i} \vec{\mathbf{j}}.\vec{\varphi}_{i7} = \dfrac{\partial \rho}{\partial t}. \end{cases}$$

7.2.1 Uniform grids : comparison between PML and first order condition

We first consider a computational domain of $40 \times 40 \times 40$ cubic cells of size of 5 cm. This mesh includes the PML layer which is eight cells large. Following Berenger [1], we use a parabolic profile of the conductivity and a normal reflection parameter $R(0)$ equal to 0.01%. The results computed using PML are compared to those obtained using the first order absorbing condition described in 2.4. We recall that the PML requires in the layer twice as much

degrees of freedom as the Maxwell's discretization. To compare, we consider a domain of $48 \times 48 \times 48$ cells bounded by the first order condition. The size of the cells is always 5 cm. Thus, using either the PML or the first order condition results in the similar numbers of degrees of freedom. We report on figure 8 the time evolution of the field H_x compared to the exact solution at a point located 10 cells away from the dipole and 2 cells from the PML layer. Using PML, the result is in a very good agreement with the analytical solution whereas reflections disturb the solution computed using the first order condition. To achieve the same precision, we have to use a a computational domain of $60 \times 60 \times 60$ cells. Then, using PML is about 50% cheaper in memory requirement.

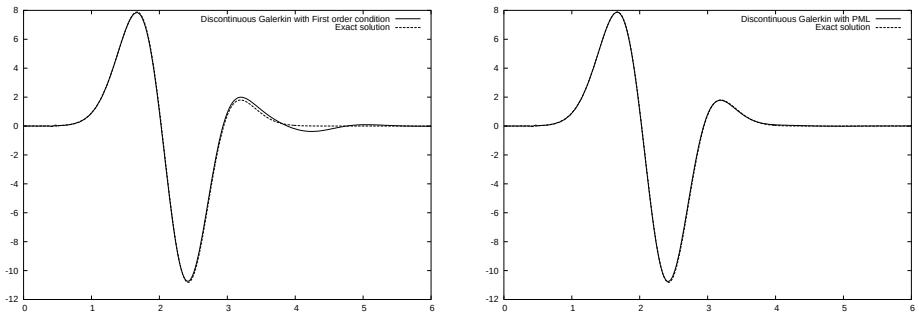

(a) First order absorbing condition

(b) PML

Figure 8: First order condition vs PML : Time evolution of H_x in a uniform grid

7.2.2 Non-conforming refined grids

We consider the same mesh as previously ($40 \times 40 \times 40$ cells including a PML layer of eight cells) and refine locally in a non-conforming way a small zone of the grid (see figure 9) with a refinement rate equal to 8. We show on figure 10 the time evolution of the fields H_x and E_y at a point of the fine grid compared to the exact solution. One can see that the error is very small although the refinement rate is very high.

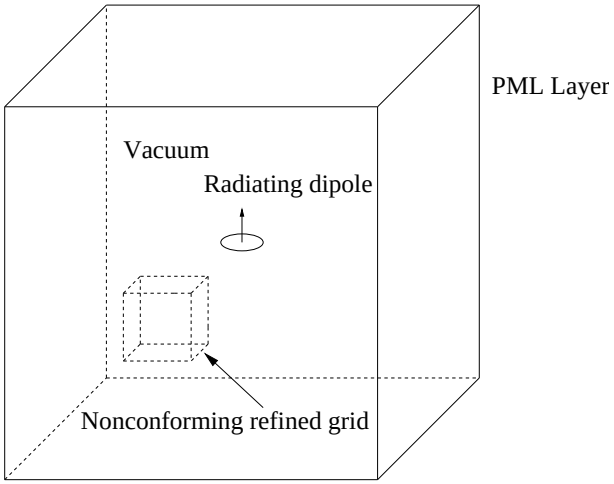

Figure 9: Diagram simulation

To show the amount of spurious reflections between the two grids, we plot on figure (11) the time evolution of the discrete energy in the fine grid compared to its variation on an equivalent uniform mesh. As we can see on the figure, the two energies are very similar which means that the spurious reflections if they exist are very small.

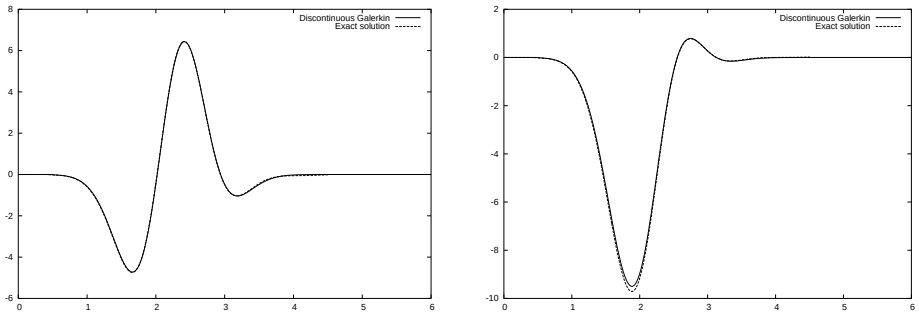

(a) Field H_x (b) Field E_y

Figure 10: Time evolution at a point of the fine grid : Refinement rate = 8

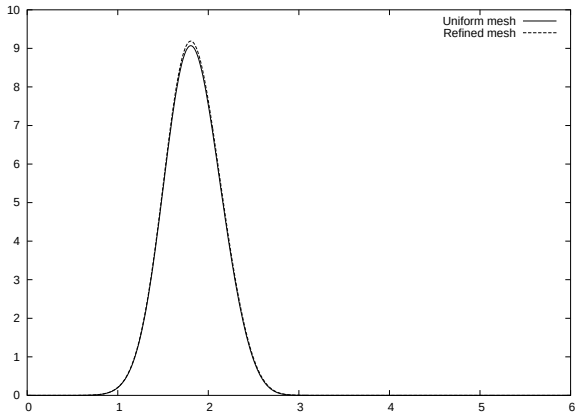

Figure 11: Evolution of the discrete energy on the fine grid (refinement rate = 8) compared to the uniform mesh

7.3 Shelter with an aperture

We consider a metallic shelter with an aperture located in the vacuum. The size of the aperture is small compared to the wavelength λ of the incident wave (see figure 12). The incident wave is a gaussian. We report the results obtained with several discretizations: a uniform coarse mesh, a coarse mesh with a non-conforming refinement (rate refinement equal to 2) around the aperture and a uniform fine grid. More precisely, the characteristics of the three simulations are

- Uniform coarse mesh ($\simeq$ 15 points by λ)
  - 18 000 elements
  - 108 000 unknowns
  - Time step: Δt
- Uniform fine mesh ($\simeq$ 30 points by λ)
  - 144 000 elements
  - 864 000 unknowns
  - Time step: Δt / 2
- Non-conforming refined mesh ($\simeq$ 15 points by λ in the coarse subgrid, $\simeq$ 30 points by λ in the fine subgrid)
  - 19 680 elements (17 760 on the coarse subgrid and 1920 on the fine subgrid)
  - 119 496 000 unknowns (only 236 $\mathbb{P}^2_{div}$ elements)

– Time step: Δt / 2

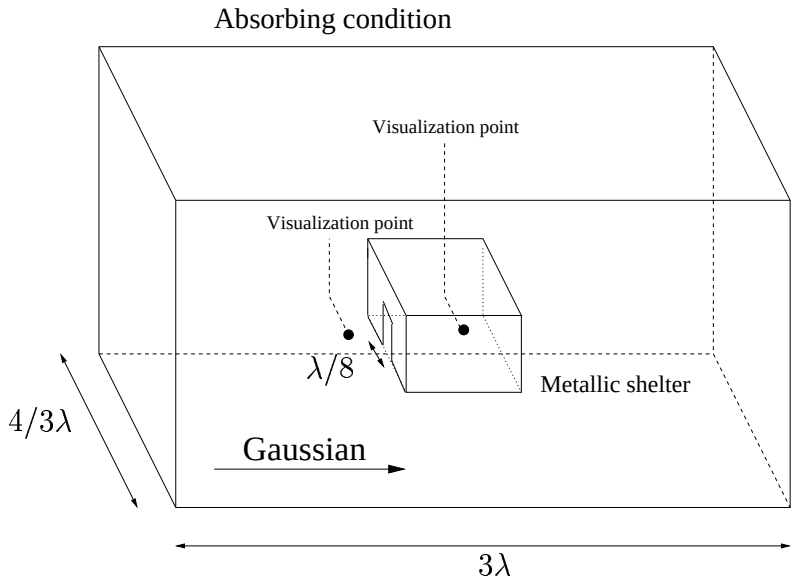

Figure 12: Diagram simulation

We report on the figure 13 the jump of the component H_y on the surface of the shelter for the three discretizations. We can see that around the aperture, the coarse mesh is not able to compute accurately the solution. If we refine locally around the aperture, the results are very similar to the results obtained with the fine mesh on the whole domain.

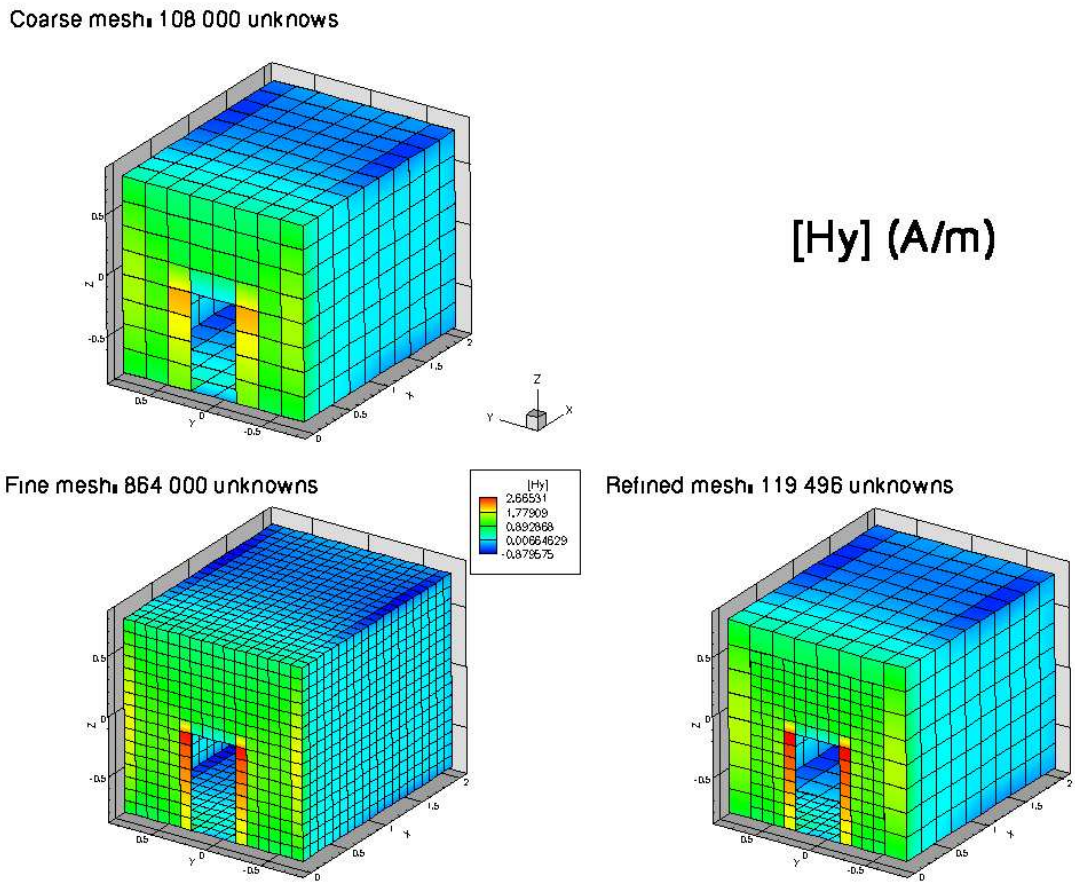

Figure 13: Jump of H_y on the shelter's surface

We show on the figure 14 the time evolution of the component E_z at a point outside the shelter close to the aperture and at a point inside the shelter. The coarse mesh solutions are again inaccurate whereas there is a very good agreement between the locally refined mesh solutions and the fine mesh ones. The locally refined discretization is seven times less costly than the fine mesh discretization.

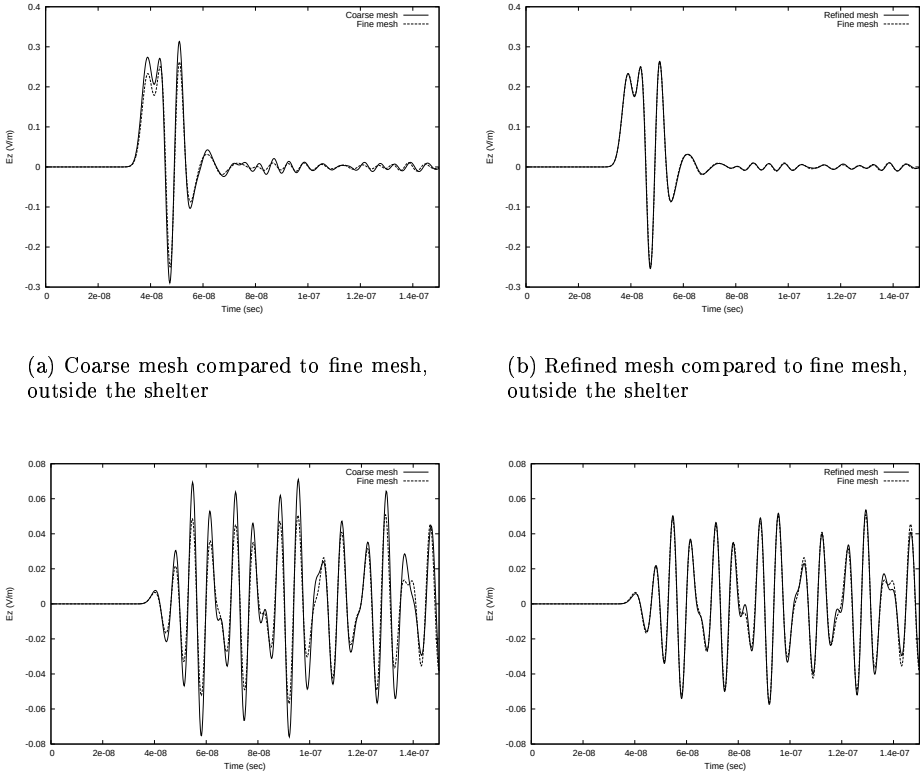

(a) Coarse mesh compared to fine mesh, outside the shelter

(b) Refined mesh compared to fine mesh, outside the shelter

(c) Coarse mesh compared to fine mesh, inside the shelter

(d) Refined mesh compared to fine mesh, inside the shelter

Figure 14: Time evolution of E_z

To show that the scheme is able to deal with high rate refinement, we propose to refine around the aperture with a rate refinement equal to eight. Because we only increase the degree of the approximation on the cells which belongs to the interface between the subgrids and the coarse subgrid, the number of $\mathbb{P}^2_{div}$ elements is the same that the number required with a rate refinement equal to two. This leads us to deal with 845 256 unknowns. Using a fine mesh on the whole domain will lead to 55 296 000 unknowns which is far beyond the computation power we dispose of. Thus, we can only compare the results obtained with the refined mesh to the results obtained with the previous fine grid ($\simeq$ 30 points by λ, 864 000 unknowns). We report on the figure 15 the time evolution of E_z at a point outside the shel-

ter close to the aperture and at a point inside the shelter. The solutions are very comparable.

- Nonconforming refined mesh (rate = 8, $\simeq$ 15 points by λ in the coarse subgrid, $\simeq$ 120 points by λ in the fine subgrid)
  - 140 640 elements (17 760 on the coarse subgrid and 122 880 on the fine subgrid)
  - 845 256 unknowns (only 236 $\mathbb{P}^2_{div}$ elements)
  - Time step: $\Delta t/8$
  - Equivalent uniform mesh: 55 296 000 unknowns

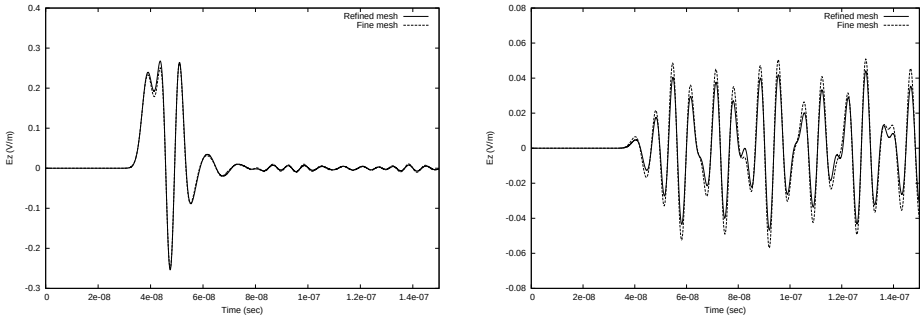

(a) Outside the shelter

(b) Inside the shelter

Figure 15: Time evolution of E_z, fine mesh compared to refined mesh: rate refinement = 8

8 Conclusion

We have described a fully explicit Discontinuous Galerkin method which has been applied to solve Maxwell equations on both conforming and nonconforming grids. The scheme conserves a discrete energy and is stable under a CFL condition. We have shown that numerical dispersion errors do not increase significantly when using small time steps as it is the case for **FDTD** schemes for example. The numerical experiments we carried out revealed the high quality of the results together with the flexibility of the method allowing us to mix different sets of local basis functions, to use PML or upwinding techniques at absorbing boundaries and finally to use highly refined grids without a noticeable loss of precision.

References

[1] J-P. Berenger, *Three-Dimensionnal Perfectly Matched Layer for the Absorption of Electromagnetic Waves* Journal of computational Physics 127, 363-379 (1996)

[2] B. Cockburn, G.E. Karniadakis and C-W. Shu, *The Development of Discontinuous Galerkin Methods*, Lecture Notes in Computational Science and Engineering, volume 11, Springer, 2000.

[3] G. Cohen, X. Ferrieres, P. Monk, S. Pernet, *Mass-Lumped Edge Elements for the lossy Maxwell's equations*, Mathematical and Numerical Aspects of Wave Propagation, 383-388, Springer, 2003.

[4] T. Fouquet, *Raffinement de maillage spatio-temporel local pour les équations de Maxwell*, Thèse, Paris IX Dauphine, Juin 2000.

[5] S. Piperno, M.Remaki, L.Fezoui, *A non-diffusive finite volume scheme for the 3D Maxwell equations on unstructured meshes*, SIAM J. Numer. Anal., vol. 39, No. 6, pp. 2089-2108, (2002)

[6] S. Piperno, L. Fezoui, *A centered Discontinuous Galerkin Finite Volume scheme for the 3D heterogeneous Maxwell equations on unstructured meshes* Rapport Inria No 4733, 2003.

[7] M. Remaki et L. Fezoui, *Une méthode de Galerkin Discontinu pour la résolution des équations de Maxwell en milieu hétérogène*, rapport de recherche INRIA no 3531, janvier 1998.

[8] K.S. Yee, *Numerical Solution of initial boundary value problem involving Maxwell's equations in isotropic media.* IEEE Trans. Ant. Propagat., Vol AP14, 1966.

Unité de recherche INRIA Sophia Antipolis
2004, route des Lucioles - BP 93 - 06902 Sophia Antipolis Cedex (France)

Unité de recherche INRIA Futurs : Parc Club Orsay Université - ZAC des Vignes
4, rue Jacques Monod - 91893 ORSAY Cedex (France)
Unité de recherche INRIA Lorraine : LORIA, Technopôle de Nancy-Brabois - Campus scientifique
615, rue du Jardin Botanique - BP 101 - 54602 Villers-lès-Nancy Cedex (France)
Unité de recherche INRIA Rennes : IRISA, Campus universitaire de Beaulieu - 35042 Rennes Cedex (France)
Unité de recherche INRIA Rhône-Alpes : 655, avenue de l'Europe - 38334 Montbonnot Saint-Ismier (France)
Unité de recherche INRIA Rocquencourt : Domaine de Voluceau - Rocquencourt - BP 105 - 78153 Le Chesnay Cedex (France)

Éditeur
INRIA - Domaine de Voluceau - Rocquencourt, BP 105 - 78153 Le Chesnay Cedex (France)
http://www.inria.fr
ISSN 0249-6399